INTERNATIONAL JOURNAL FOR NUMERICAL METHODS IN FLUIDS, VOL. 14, 981–1003 (1992)

BOUNDARY-CONFORMING MAPPING APPLIED TO COMPUTATIONS OF HIGHLY DEFORMED SOLIDIFICATION INTERFACES

K. TSIVERIOTIS AND R. A. BROWN

Department of Chemical Engineering, Massachusetts Institute of Technology, Cambridge, MA 02139, U.S.A.

SUMMARY

A new boundary-conforming mapping is developed for the calculation of highly deformed cellular solidification interfaces in a model of directional solidification of a binary alloy. The mapping is derived through a variational fomulation that is designed so that the grid penetrates the grooves between cells along the interface without causing a loss of ellipticity of the mapping equations. A finite element/Newton method is presented for simultaneous solution of the free boundary problem described by the solutal model of directional solidification and the mapping equations. Results are compared to previous calculations and demonstrate the importance of accurate representation of the interface shape for understanding the solution structure.

KEY WORDS Co-ordinate mapping Finite element method Free-boundary Solidification

1. INTRODUCTION

Complex cellular and dendritic microstructures form during directional solidification of a binary alloy as a result of interactions between the interface morphology and the solute and temperature fields in the surrounding melt and solid. These morphological transitions are readily observed in the interface in a thin sample of a binary alloy that is translated at constant speed through an externally imposed temperature gradient as shown in Figure 1. As the melt solidifies, solute is rejected into the melt according to the phase diagram of the alloy. Diffusion in the melt cannot disperse this solute and an enriched layer forms in the melt adjacent to the interface. The melting point of the material is increased and, if the temperature is lower than the melting temperature in the enriched melt, irregular solidification occurs, giving rise to non-planar melt/solid interface shapes. This explanation is the basis of the *constitutional supercooling mechanism*[1] for the onset of solidification microstructure.

Experimental observations of approximately two dimensional microstructures[2,3] show the evolution of cellular and dendritic structures following the onset of instability of the planar interface. The goal of numerical solution of models for microstructural solidification is to compute the evolution of these structures as a function of operating conditions, e.g. temperature gradient, solidification rate and thermophysical properties.

The continuum solidification models used to model microstructure formation consist of transport equations for solute and energy in the melt and the solid and interfacial conditions that relate the temperature and concentration fields to the shape of interface. The models consist of field equations for diffusion of solute and heat, boundary conditions for conservation of these

0271–2091/92/080981–23$11.50

Received 20 February 1991
Revised 20 August 1991

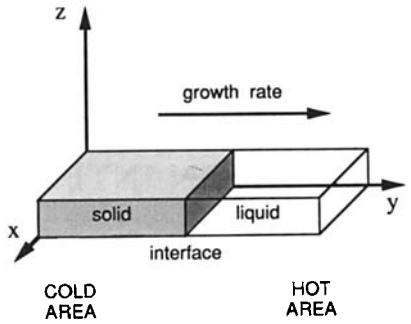

Figure 1. Schematic drawing of directional solidification of a thin film of a binary alloy. The solid grows in the y-direction as the sample moves with constant velocity in this direction from the hot to the cold area.

quantities at the interface and conditions for thermodynamic equilibrium at the interface. Most important is the Gibbs–Thomson equation[4] that relates the melting temperature to the concentration and the curvature of the interface. The onset of cellular solidification is predicted by linear stability analysis[5] of this set of equations, which yields the value of the control parameter, either growth rate or temperature gradient, for the onset of small amplitude cells as a function of the cellular wavelength. Weakly non-linear analyses[6,7] of finite amplitude cells predict shapes that evolve with a specified wavelength from the critical value of the control parameter.

Numerical methods for solving these free and moving boundary problems that describe microstructure formation must compute simultaneously the field variables and the interface shape. The coupling between the interface shape and the field variables introduces implicit non-linearities through the boundary conditions that are imposed on the free surface and must be addressed by any algorithm for numerical solution. Ettouney and Brown[8] classified methods for numerical solution of free boundary problems by whether the equations are solved in the physical domain or on a transformed space, by the iterative method used to account for the non-linearity introduced by the free boundary and by the interface condition that is distinguished to compute the interface.

Co-ordinate transformation methods offer a powerful way of making explicit the non-linear dependence of the field equations on the unknown interface shape. Here the unknown boundary shape is taken into account explicitly through a mapping that transforms the melt and solid regions to a new domain with fixed boundaries, one of which corresponds to the mapped free boundary. The functional representation of the free boundary appears explicitly in the transformed field equations and boundary conditions and hence is readily treated by non-linear iterative methods applied to the numerical discretization of the equation set.[8]

It is clear that the success of such methods hinges on the ability of the mapping to represent highly distorted boundary shapes. Mapping methods have been successfully developed for the solution of a variety of free boundary problems with specific types of interface shapes, including coating flows[9,10] and flows around drops and bubbles.[11–13] These mapping methods can be classified according to the categories introduced by Thompson *et al.*[14,15] as either algebraic methods which relate the physical and transformed domains according to simply algebraic expressions or smooth, orthogonal and variational methods which require the solution of partial differential equations for construction of the transformed co-ordinates. Each method varies in its ability to control key elements of the co-ordinate transformation: the smoothness of the mapping, the orthogonality of the transformed co-ordinate curves and the concentration of the co-ordinate curves in the domain.

Each of these measures sets constraints on the development of a satisfactory mapping method for computation of cellular microstructures in directional solidification because of the extreme variations in interface shape that can occur with changes in operating conditions, e.g. temperature gradient and growth rate. As the depth of the cell increases, the mapping must remain smooth, nearly orthogonal and control the distribution of the co-ordinate curves. No single mapping method has been developed that accomplishes these goals for the transition between shallow and deep solidification cells. This is the objective of the new mapping method presented here.

Ungar and Brown[7] first computed the evolution of two-dimensional steadily solidifying cellular structures that evolve from the planar solidification front. These calculations were based on the isotherm/Newton method.[8] Here the Galerkin finite element method is used to discretize the field equations and Gibbs–Thomson equation which are written in a transformed co-ordinate system that is defined by an algebraic mapping written in terms of the Cartesian Monge representation $y=h(x)$ for the interface; the mapping and the Monge representation are shown schematically in Figure 2(a). The Gibbs–Thomson equation is *distinguished* as the condition defining the interface shape function $h(x)$. The algebraic co-ordinate transformation makes the field equations explicitly non-linear in $h(x)$. The non-linear algebraic equations that result from the Galerkin formulation are solved by Newton's method.[8]

Although the finite element analysis using the Monge representation is very useful for calculation of shallow solidification cells and has been extended to transient analysis of single[16] and collections of cells,[17] it is not applicable to calculations of deep cellular structures. Solidification cells often develop deep and narrow grooves, $|\partial h/\partial x| \gg 1$, or even re-entrant shapes that cannot be represented by the Monge co-ordinate representation. This shortcoming is most obvious in the examination by Wheeler and Winters[18] of the calculations of Ungar and Brown.[7]

Ungar and Brown[19] realized this shortcoming and generalized the isotherm/Newton formulation to an algebraic mapping method that represents region of a deep cellular structure by patches of Cartesian and polar Monge representations; this mapping is shown schematically in Figure 2(b). Deep cellular structures were successfully computed using this numerical method[19,20] and were linked to calculations using the Cartesian representation by transforming solutions between the two representations. Although satisfactory for many analyses, this methodology fails in steady state and dynamical studies of cells that evolve from shallow to deep

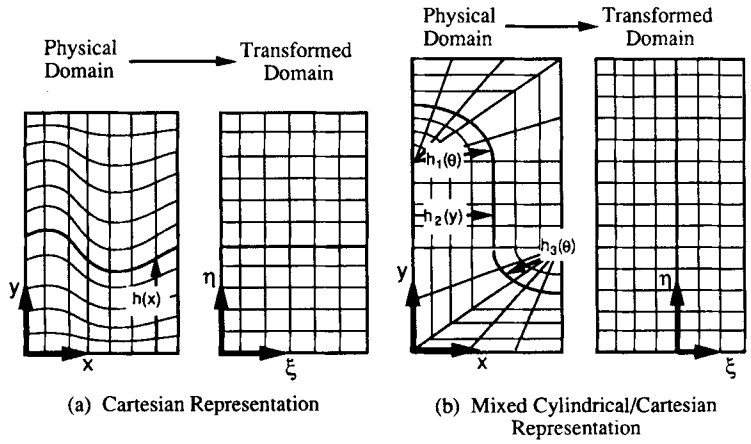

Figure 2. (a) Cartesian algebraic mapping of the solidification domain using the Monge representation for the interface. (b) Polar/Cartesian algebraic mapping of the region occupied by half a solidification cell.

and simultaneously alter the cellular wavelength, by either tip splitting of a single cell or by squeezing out a cell along a front.

Ungar and Brown[7] used the Newton/isotherm finite element method and the Cartesian Monge representation to compute with decreasing temperature gradient the non-linear evolution of families of steady state cells within a sample with prescribed wavelength λ. One of the most interesting discoveries of this study was the existence of a secondary bifurcation with a family of cells with half the original wavelength, $\lambda/2$. This bifurcation behaviour, shown in Figure 4 of Ungar and Brown[7] and in Figure 12 of this work, was linked by Ungar and Brown to the existence of a codimension-two bifurcation point for samples with a particular size, where the families of λ and $\lambda/2$ cells bifurcate simultaneously from the planar solution. For calculations with sample sizes close to this critical dimension, the secondary bifurcation occurs for small amplitude cells that are well represented by the Cartesian Monge method.

However, Wheeler and Winters[18] demonstrated that the calculations by Ungar and Brown[7] with larger amplitude cells *are not* reproducible. Attempts to refine the mesh yielded varying solution structures. We show here that these results are the direct outcome of the failure of the Cartesian Monge representation and demonstrate that the cell shapes are re-entrant. Calculations with a model that includes the physics appropriate for re-entrant cells and uses a new mapping method yield the secondary bifurcations for deep cells and converge with mesh refinement.

2. SOLUTAL MODEL FOR DIRECTIONAL SOLIDIFICATION

We consider the two-dimensional directional solidification of a dilute binary alloy. The computational domain is shown in Figure 3 and consists of portions of the melt and solid of lateral extent L and length $l=l_m+l_s$. The solutal model (SM) for morphological instability accounts for the evolution of the solute concentration field and the position of the free melt/solid interface, but assumes that the temperature field is linear in the direction of growth and that it is unaffected by changes in the interface shape. These are good approximations when the thermal conductivities in the melt and solid are equal, convective heat transfer is negligible and latent heat release is

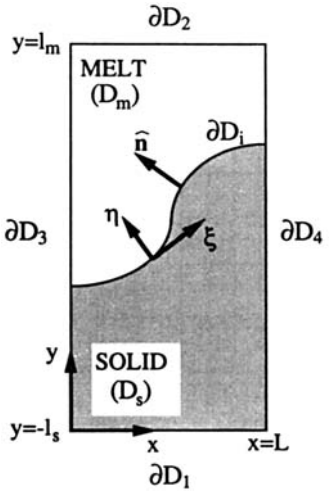

Figure 3. Computational domain for the two-sided solutal model.

insignificant. Under such conditions the thermal field is mathematically decoupled from the solutal field and the interface shape.

Dimensionless variables are defined by scaling lengths with a characteristic length L_0, time with the diffusion time $\tau_d = L_0^2/\mathscr{D}_m$, where $\mathscr{D}_m$ is the solute diffusivity in the melt, temperature with the melting temperature of pure material, T_m^0, and concentration with the bulk concentration of the alloy, c_∞. Quantities referring to the melt and solid phases are denoted by the subscripts 'm' and 's', respectively.

The dimensionless solute conservation equations in the melt and solid are written in the laboratory reference frame as

$$\frac{\partial c_m}{\partial t} = \nabla^2 c_m + P(\hat{\mathbf{e}}_y \cdot \nabla c_m), \tag{1}$$

$$\frac{\partial c_s}{\partial t} = R_m \nabla^2 c_s + P(\hat{\mathbf{e}}_y \cdot \nabla c_s), \tag{2}$$

where $R_m \equiv \mathscr{D}_s/\mathscr{D}_m$ is the ratio of solutal diffusivity in the solid to that in the melt and $P \equiv L_0 V/\mathscr{D}_m$ is the solutal Peclet number, expressing the importance of solutal diffusion transport relative to the uniaxial convection of solute caused by translation of the sample in the y-direction.

The melt/solid interface is assumed to be a Gibbs dividing surface,[4] meaning that the interface ∂D_I is a two-dimensional boundary separating two continuous phases. Here it is assumed that the interface is described by a general parametrization of the form $F(x, y, t)=0$, where $F>0$ in the melt and $F<0$ in the solid. The solute balance at the interface gives

$$\hat{\mathbf{n}} \cdot \nabla c_m - R_m \hat{\mathbf{n}} \cdot \nabla c_s = (c_m - c_s)\left(- P\hat{\mathbf{e}}_y \cdot \hat{\mathbf{n}} + \left[\frac{1}{|\nabla F|} \frac{\partial F}{\partial t} \right]_{F=0} \right) \quad \text{at } \partial D_I, \tag{3}$$

where $\hat{\mathbf{n}}$ is the unit vector normal to the interface pointing into the melt,

$$\hat{\mathbf{n}} \equiv \left[\frac{\nabla F}{|\nabla F|} \right]_{F=0}. \tag{4}$$

In addition, local thermodynamic equilibrium at the interface is used to relate the composition of melt and solid at the interface as

$$c_s = k c_m \quad \text{at } \partial D_I, \tag{5}$$

where k is the solute partition coefficient. The effect of concentration and curvature on the melting temperature is accounted for by the Gibbs–Thomson equation[4] as

$$T = 1 + m/k + Gy = 1 + mc_m + 2\mathscr{H}\Gamma \quad \text{at } \partial D_I, \tag{6}$$

where G is the dimensionless temperature gradient, $\mathscr{H}$ is the local mean curvature of the interface and m is the dimensionless slope of the liquidus line. The dimensionless capillary constant $\Gamma \equiv \tilde{\Gamma}/L_0$ is defined in terms of the capillary length $\tilde{\Gamma}$, which is the ratio of the surface energy γ of the melt/solid interface to the latent heat of fusion, ΔH_f, i.e. $\tilde{\Gamma} \equiv \gamma/\Delta H_f$. We assume that γ is homogeneous and isotropic. For the interface parametrization $F(x, y, t)=0$, the curvature is given by[21]

$$2\mathscr{H} \equiv -\nabla_s \cdot \hat{\mathbf{n}},$$

where $\nabla_s = (\mathbf{I} - \hat{\mathbf{n}}\hat{\mathbf{n}}) \cdot \nabla$ is the surface gradient operator and $\mathbf{I}$ is the identity tensor. For a two-dimensional interface an alternative expression for the curvature is

$$2\mathscr{H} = \frac{d\phi}{ds}, \tag{7}$$

where ϕ is the angle formed by the unit vector tangent to the interface and pointing in the direction of increasing interfacial arc length and the unit vector $\hat{\mathbf{e}}_x$. Expression (7) is particularly convenient for the finite element approximations used here because it leads directly to the weak fomulation of the Gibbs–Thomson equation as discussed in Section 4. Others[22] have made use of this advantage in the solution of viscous free surface flows.

The far-field conditions for the solute concentration are based on a global solute balance for the finite domain (see Figure 3) and are

$$\hat{\mathbf{e}}_y \cdot \nabla c_m = P(1 - c_m) \quad \text{at } \partial D_2, \tag{8}$$

$$\hat{\mathbf{e}}_y \cdot \nabla c_s = 0 \quad \text{at } \partial D_1, \tag{9}$$

where diffusion in the solid far from the interface is neglected. Reflective symmetry conditions are assumed for the concentration and the interface shape at the lateral boundaries of the domain:

$$\hat{\mathbf{e}}_x \cdot \nabla c_m = 0 \quad \text{and} \quad \hat{\mathbf{e}}_x \cdot \nabla c_s = 0 \quad \text{at } \partial D_3, \partial D_4, \tag{10}$$

$$\phi = 0 \quad \text{at } \partial D_3, \partial D_4, \tag{11}$$

where condition (11) specifies the reflective symmetry of the interface.

Equations (1)–(11) constitute the solutal model (SM) of directional solidification in two dimensions. The SM is characterized by the six non-dimensional parameters k, m, P, R_m, Γ and G. This model is called the two-sided SM because diffusion in both phases is included. The one-sided SM results when solute diffusion in the solid is neglected ($R_m = 0$).

Although setting $R_m = 0$ and removing the solute transport problem in the solid phase from the solidification model halves the size of the modelling problem, this one-sided model is severely limited in the range of cell shapes for which it is appropriate. More precisely, neglecting transport in the solid phase restricts the one-sided model from correctly describing solute transport in cells with re-entrant grooves, like the one shown in Figure 4. Consider material that translates along

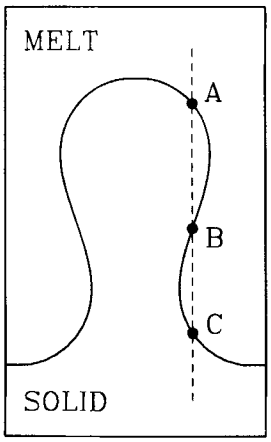

Figure 4. Schematic showing a solidification cell with re-entrant grooves.

the dashed line in Figure 4. Material solidifies at the melt/crystal interface (A), moves through the solid, remelts in the groove (B) and resolidifies at the groove bottom (C). Modelling of re-entrant cells requires computing the concentration in the solid that links the concentration at points A and B in Figure 4. Setting $R_m = 0$ and neglecting the solute transport equation (2) destroys this information in the solutal model. Ungar and Brown[19] realized this important point and first included solid phase solute transport in the solutal model. Others[23] have neglected this important coupling.

While typical thin film directional solidification systems have large lateral dimensions, we confine our calculations to samples of the order of the most dangerous wavelength from the appropriate neutral stability curve, i.e. the wavelength λ_c corresponding to minimum P (for fixed G) or maximum G (for fixed P) for the onset of cellular forms. This approach has been used in other calculations.[7,17]

3. DEVELOPMENT OF A NEW BOUNDARY-CONFORMING MAPPING METHOD

3.1. Background

Generally, the mapping problem for a three-dimensional region consists of finding the transformed co-ordinates $\xi^i(x^1, x^2, x^3)$, $i = 1, 2, 3$, which describe a one-to-one mapping of each point (x^1, x^2, x^3) of the *physical* domain onto a point (ξ^1, ξ^2, ξ^3) of a *transformed* domain. Boundary-conforming mappings require the boundaries of the physical domain to coincide with co-ordinate lines of the transformed domain; the two-dimensional boundary-conforming mapping problem is shown schematically in Figure 5.

Valuable insight into the mapping problem comes from realizing that the construction of a curvilinear co-ordinate is equivalent to determining the components of the metric tensor $\mathbf{G}$ as

$$G_{ij} = \mathbf{r}_i \cdot \mathbf{r}_j = \frac{\partial \mathbf{r}}{\partial \xi^i} \cdot \frac{\partial \mathbf{r}}{\partial \xi^j} \tag{12}$$

and that the independent components $\{G_{ij}\}$ of the metric tensor are the degrees of freedom of the mapping problem.[24] In a Euclidean space the metric tensor has three independent components in three dimensions and two components in two dimensions.[25] Thus three constraints are needed to specify the mapping in three dimensions and two constraints in two dimensions. These constraints are not always explicit in various mapping methods where the corresponding degrees of

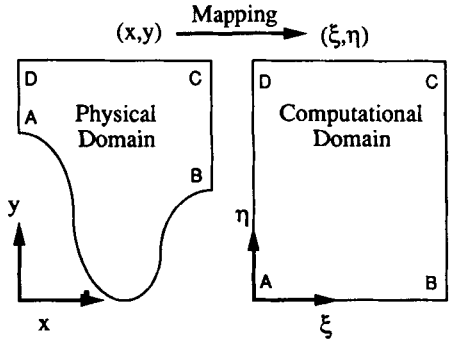

Figure 5. Schematic representation of boundary-conforming mapping between points in the physical domain (x, y) and points in the computational domain (ξ, η).

freedom are distributed over a larger number of weaker equations and boundary conditions. In our formulation the transformed co-ordinate lines are used to discretize the domain in quadrilateral finite elements.

Three characteristics are used to quantitatively describe a mapping: smoothness, orthogonality and mesh concentration. A two-dimensional curvilinear co-ordinate system becomes smoother as the magnitude of the gradients of the transformed co-ordinates, $|\nabla\xi|$ and $|\nabla\eta|$, decreases. The quantity $(\nabla\xi\cdot\nabla\eta)^2$ is a measure of deviation from orthogonality; another measure is introduced later in this section. Finally, mesh concentration is measured as the ratio of the area of a part of the physical domain to the area of the corresponding part in the transformed domain given by the Jacobian of the transformation, $J\equiv x_\xi y_\eta - x_\eta y_\xi$, where the subscripts denote partial differentiation, i.e. $x_\xi\equiv\partial x/\partial\xi$.

A variety of mappings have been proposed and are reviewed by Thompson *et al.*[14,15] These techniques differ in the degree of control of the smoothness, orthogonality and mesh concentration. For example, the algebraic mappings shown in Figure 2 guarantee control over the concentration of co-ordinate lines near the interface, but insure no degree of smoothness or orthogonality and therefore may result in highly deformed meshes.

Other methods for generating smooth meshes are based on solution of Laplace or Poisson equations and focus on controlling the values of $|\nabla\xi|$ and $|\nabla\eta|$ over the domain.[26] Alternatively, orthogonal mappings satisfy $(\nabla\xi\cdot\nabla\eta)^2=0$, leaving one degree of freedom for control of the co-ordinate aspect ratio $\sqrt{(g_{11}/g_{22})}$ over the domain and the values of the transformed co-ordinates on the boundaries.[24,27] Conformal mappings are the most restrictive because they require both othogonality and unit aspect ratio, allowing no degrees of freedom to control any other characteristics of the mesh. These restrictions can result in ill-conditioned conformal maps.[28]

A more efficient alternative to these methods is the development of a mapping based on optimizing a combination of the characteristics of the co-ordinate transformation; such techniques are referred to as variational methods. Brackbill and Saltzman[29] used the functionals

$$I_s = \int\int_D [(\nabla\xi)^2 + (\nabla\eta)^2]\,dx\,dy, \tag{13}$$

$$I_o = \int\int_D (\nabla\xi\cdot\nabla\eta)^2 J^3\,dx\,dy, \tag{14}$$

$$I_v = \int\int_D wJ\,dx\,dy \tag{15}$$

defined over the physical domain to describe the deviation of the mesh smoothness, orthogonality and desired concentration respectively. The mapping problem was stated as the minimization of the composite functional

$$I = I_s + \lambda_o I_o + \lambda_v I_v = \int\int_D f(x, y, \xi, \eta, \nabla\xi, \nabla\eta)\,dx\,dy, \tag{16}$$

with the corresponding Euler–Lagrange equations[30]

$$\nabla\cdot\frac{\partial f}{\partial(\nabla\xi)} = \frac{\partial f}{\partial\xi}, \qquad \nabla\cdot\frac{\partial f}{\partial(\nabla\eta)} = \frac{\partial f}{\partial\eta}. \tag{17}$$

The set of second-order partial differential equations (17) for $x(\xi,\eta)$ and $y(\xi,\eta)$ are the mapping equations, in which the relative importance of orthogonality, smoothness and mesh concentra-

tion is set by the weighting factors λ_0 and λ_γ. The mesh spacing is also varied according to the preset or solution-dependent function w in (15).

Kreis *et al.*[31] pointed out that the formulation (16) involves dimensionally inhomogeneous terms and rescaling of the weighting should be done for consistent control of the grid properties. To avoid such rescaling, Christodoulou and Scriven[10] introduced a new orthogonality functional which scales with the smoothness. They used a measure for deviation from orthogonality based on the generalized Cauchy–Riemann conditions $S\xi_x=\eta_y$ and $S\xi_y=-\eta_x$. Their orthogonality functional is

$$I_0'=\int\int_D\left[\left(\sqrt{(S)}\xi_x-\frac{1}{\sqrt{S}}\eta_y\right)^2+\left(\sqrt{(S)}\xi_y+\frac{1}{\sqrt{S}}\eta_x\right)^2\right]dx\,dy, \tag{18}$$

with ξ, η and S as the unknown functions. The Euler–Lagrange equations corresponding to this functional are

$$\nabla\cdot(S\nabla\xi)=0, \qquad \nabla\cdot\left(\frac{1}{S}\nabla\eta\right)=0, \qquad S=\sqrt{\left(\frac{x_\xi^2+y_\xi^2}{x_\eta^2+y_\eta^2}\right)}. \tag{19}$$

On the basis of this orthogonality functional, Christodoulou and Scriven proposed the mapping equations

$$\nabla\cdot\left[\sqrt{\left(\frac{x_\xi^2+y_\xi^2}{x_\eta^2+y_\eta^2}\right)}+\varepsilon\right]\nabla\xi+\frac{\varepsilon_1}{J}\frac{\partial}{\partial\xi}\ln[(x_\xi^2+y_\xi^2)f(\xi)]=0, \tag{20}$$

$$\nabla\cdot\left[\sqrt{\left(\frac{x_\eta^2+y_\eta^2}{x_\xi^2+y_\xi^2}\right)}+\varepsilon\right]\nabla\eta+\frac{\varepsilon_2}{J}\frac{\partial}{\partial\eta}\ln[(x_\eta^2+y_\eta^2)g(\eta)]=0, \tag{21}$$

where ε weights the smoothness functional relative to the orthogonality measure and ε_1 and ε_2 control the concentration of the mesh in the ξ- and η-direction respectively. The first two terms in (20) and (21) are the result of minimizing the functional $I_0'+\varepsilon I_s$ and the third term is added to control the spacing of the mesh. The fact that there is no contribution to the minimized functional to control mesh spacing and that this contribution is added after the minimization does not make (20) and (21) fundamentally different from the equations derived by Brackbill and Saltzman.[29]

Equations (20) and (21) combine several classes of mapping methods. Nevertheless, these equations are limited because their part corresponding to mesh concentration is mathematically hyperbolic. Thus high positive values of ε_1 and ε_2 result in a second-order hyperbolic equation set which, in general, is not a well-posed boundary value problem.[32] This limitation severely hinders the application of the mapping method in calculation of cellular microstructures, where the mesh must accurately describe highly distorted cell shapes. Preventing loss of ellipticity in the generation of these grids results in increased smoothness, which in turn results in meshes that do not penetrate into deep and narrow grooves. The limitations between generation of an adequate grid and loss of ellipticity of the mapping equations are demonstrated in the sample calculations that follow.

To test the robustness of the variational mapping method for calculations of cellular microstructures, we consider its application to a problem with a fixed domain that resembles a solidification cell and test the variational mapping, (20) and (21), for various degrees of deformation of this domain. The boundary conditions at the bottom boundary of the physical domain are set by requiring that the ξ-axis of the transformed domain coincides with this boundary, i.e. $\eta=0$ along the bottom. In addition, it is required that the arc length is equally distributed on the bottom boundary with respect to the co-ordinate ξ, i.e. $\xi=s(\xi)/s_0$, where s is the boundary arc length measured from $x=0$ and s_0 is the total arc length of the boundary. Reflective boundary

conditions are assumed at $y=l_m$, i.e. $\eta=$constant and $\hat{\mathbf{n}}\cdot\nabla\xi=0$, where $\hat{\mathbf{n}}$ is the unit normal to the boundary, and on the lateral sides of the domain, i.e. $\xi=$constant and $\hat{\mathbf{n}}\cdot\nabla\eta=0$. Equations (20) and (21) are solved with these boundary conditions, using Galerkin's finite element method, as detailed in Section 4 for the more general case of the coupled solidification/mapping problem.

The performance of the variational mapping is presented in Figure 6(a) for the domain around a moderately distorted boundary. Here the mesh is concentrated close to the deformed boundary by using the following expressions for $(\varepsilon_1, \varepsilon_2)$: $\varepsilon_1=0$ and $\varepsilon_2=e_2\exp(-4\eta)$. For very small values of the weight factor e_2 the mesh co-ordinate in the η-direction avoids the groove of the cell. However, as e_2 increases, the mesh concentrates close to the groove, resulting in a satisfactory mapping.

The variational mapping is less successful for highly distorted domains, as demonstrated in Figure 6(b). Here the smoothing part of the mapping equations tend to smooth out abrupt changes in the co-ordinate curves caused by the boundary shape. This effect forces the mesh to concentrate over convex boundaries and avoid concave ones. More ξ-co-ordinate lines are forced into the groove only when e_2 is increased significantly. This improves the mapping only up to the point where the equations become hyperbolic and the boundary value problem becomes ill-posed. For the interface shape shown in Figure 6(b) this occurs at $e_2\approx 0{\cdot}33$. The discretized equations cannot be solved for larger e_2. The results shown in Figure 6 were obtained without the orthogonality term in (20) and (21). Including the orthogonality constraint necessitates even higher weightings on the concentration control term for meaningful mappping results, leading to numerical failure of the mapping even for interfaces considerably less deformed than that shown in Figure 6(b). (See Note Added in Proof at the end of the paper.)

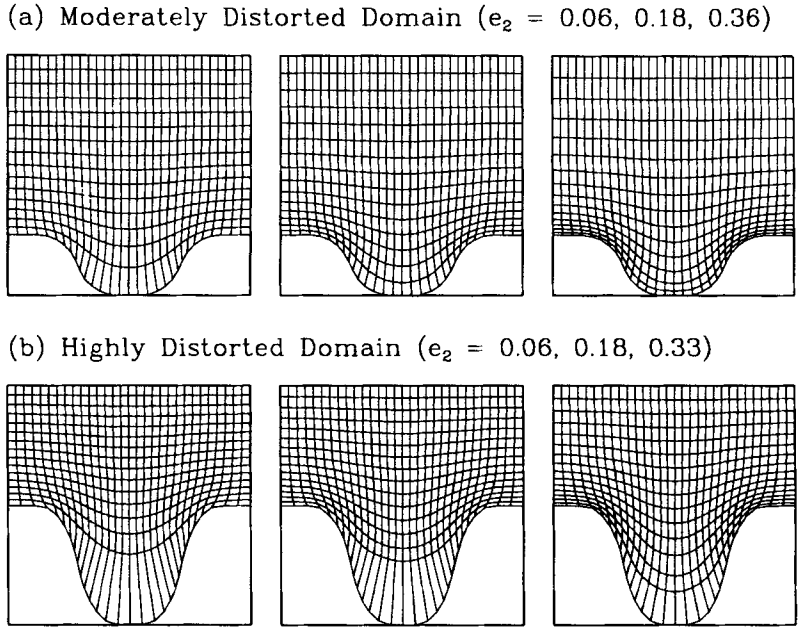

Figure 6. Sample mapping results for fixed domains using the mapping equations (20) and (21) with $\varepsilon_1=0$ and $\varepsilon_2=e_2\exp(-4\eta)$.

3.2. Mapping for deep cells

It is clear that a more specific method is needed for successful mapping of the region inside one or more highly deformed cells or any other highly distorted interfacial shape. The first step towards the development of such a method is to realize that the two sets of co-ordinate lines play different roles in free interface problems. The co-ordinate lines parallel to the interface (ξ-curves) should follow or even concentrate close to the interface, while the co-ordinate lines normal to the interface (η-curves) are simply required to intersect smoothly and orthogonally with ξ-curves.* This anisotropy in the mapping transformation is not captured by the existing variational formulations. Another important observation results from the symmetry of the problem. In order for the mapping to behave consistently for any number of interface cells, any control function used in the mapping equations should depend only on η.

A two-step methodology is proposed to develop a transformation that has these features. First, a set of ξ-curves that follow the interface as closely as possible is produced; then, keeping the ξ-curves constant, η-curves are constructed so that smoothness and orthogonality of the co-ordinate system are optimized. This decoupling is pivotal in achieving the desired control while preserving the ellipticity of the mapping equations.

In the first step a Poisson equation is written to define the η-co-ordinate as

$$\nabla \cdot (\mathbf{a} \cdot \nabla \eta) = f(\eta), \tag{22}$$

where

$$\mathbf{a} = \begin{pmatrix} 1 & 0 \\ 0 & a(\eta) \end{pmatrix}, \qquad a(\eta) \gg 1. \tag{23}$$

Here the scaling condition on $a(\eta)$ forces the extrema of the ξ-co-ordinate lines to be equidistant in the y-direction. This prevents the co-ordinate lines from concentrating over convex parts of the interface as opposed to concave portions of it. The forcing function $f(\eta)$ controls the concentration of the mesh in the η-direction; negative values of $f(\eta)$ concentrate the ξ-curves towards the interface without introducing hyperbolic terms in the mapping equations.

The second step in the development of the mapping equations is straightforward and involves minimization of the combination of orthogonality and smoothness functionals $I' = I'_o + \varepsilon(\eta) I_s$ (see (13) and (18)) with respect to ξ and S only. The second mapping equation is obtained as the Euler–Langrange equation for the functional I' as

$$\nabla \cdot \left[\sqrt{\left(\frac{x_\xi^2 + y_\xi^2}{x_\eta^2 + y_\eta^2} \right)} + \varepsilon(\eta) \right] \nabla \xi = 0. \tag{24}$$

Equations (22) and (24) are the proposed mapping equations. Since this method involves combining smooth and variational parts, we refer to it as the 'mixed mapping method' (MMM).

Calculations for sample domains using the MMM have been performed to compare it with the variational mapping method described by (20) and (21). The test problem is the same one as used in Figure 6. Mappings generated by solution of (22) and (24) using the finite element method with no spacing control ($f(\eta) = 0$), $\varepsilon = 0{\cdot}2$ and $a(\eta) = 100$ are shown in Figure 7(a). Here the ability of the MMM to follow the interface with increasing depth is clear. Mappings generated with increasingly narrow and re-entrant cells are shown in Figure 7(b). In this case spacing control was

* Co-ordinate curves with η = constant and ξ = constant are referred to as ξ-curves and η-curves respectively.

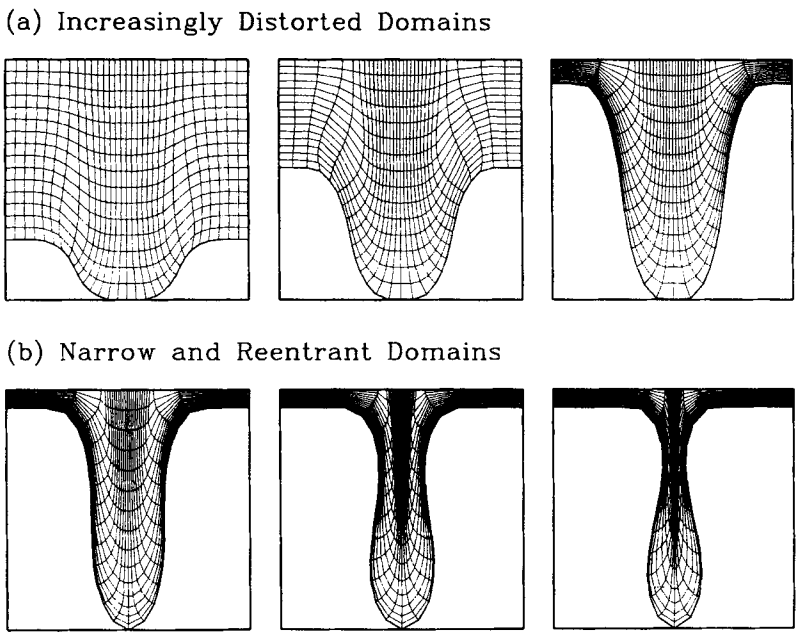

Figure 7. Sample mapping results for fixed domains using the mixed mapping method of (22) and (24). The two sequences of results show the performance of the mapping as (a) the cell depth is increased and (b) the cell becomes both narrow and re-entrant.

implemented by incorporating a forcing function of the form $f(\eta) = -1000\exp(-7\eta)$ to concentrate the ξ-curves close to the distorted boundary. It is apparent from Figure 7(b) that the MMM consistently represents increasingly narrow and re-entrant domains.

The MMM equations are used for the representation of the solidification domain shown in Figure 3. For this case the boundary conditions are similar to the ones used for the test problem. The melt/solid interface coincides with the η-axis of the transformed co-ordinate system, while the arc length is equidistributed with respect to ξ:

$$\eta = 0 \quad \text{and} \quad \xi = \frac{\int_0^{\xi} \sqrt{(x_{\xi'}^2 + y_{\xi'}^2)}\,\mathrm{d}\xi'}{\int_0^1 \sqrt{(x_{\xi'}^2 + y_{\xi'}^2)}\,\mathrm{d}\xi'} \quad \text{at } \partial D_1. \tag{25}$$

Orthogonality boundary conditions are assumed on the other domain boundaries:

$$\hat{\mathbf{e}}_y \cdot \nabla\xi = 0 \quad \text{and} \quad \eta = 1, -1 \quad \text{at } \partial D_1, \partial D_2, \tag{26}$$

$$\hat{\mathbf{e}}_x \cdot \nabla\eta = 0 \quad \text{and} \quad \xi = 0, 1 \quad \text{at } \partial D_3, \partial D_4. \tag{27}$$

4. FINITE ELEMENT/NEWTON FORMULATION OF THE SOLIDIFICATION/MAPPING PROBLEM

The steady free boundary problem for cellular solidification, (1)–(11), is solved simultaneously with the mapping equations (22) and (24) and boundary conditions (25)–(27) to compute the concentration fields $\{c_m(\xi, \eta), c_s(\xi, \eta)\}$ and the co-ordinate transformations $\{x(\xi, \eta), y(\xi, \eta)\}$ as a function of the parameters. The shape of the interface is recovered in parametric form as $x = x(\xi, \eta = 0)$ and $y = y(\xi, \eta = 0)$ for $0 \leqslant \xi \leqslant 1$. The Galerkin finite element formulation of the discrete problem is presented below.

Following Ungar *et al.*,[16] we introduce a new concentration variable defined over the solidification domain $D \equiv D_m \cup D_s$, namely

$$C(x, y) \equiv \begin{cases} c_m(x, y) & (x, y) \in D_m, \\ c_s(x, y)/k, & (x, y) \in D_s. \end{cases} \tag{28}$$

The solute field $C(x, y)$ is approximated on D in terms of Lagrangian biquadratic basis functions $\{\Phi^i\}$ as

$$C(\xi, \eta) = \sum_{i=1}^{N} C_i \Phi^i(\xi, \eta), \tag{29}$$

where $\{C_i\}$ are unknown algebraic coefficients and N is the total number of basis functions. Similarly, the co-ordinates of the physical domain are approximated in terms of unknown coefficients $\{x_i, y_i\}$ and Lagrangian bilinear basis functions $\{\Psi^i(\xi, \eta)\}$ as

$$\begin{bmatrix} x(\xi, \eta) \\ y(\xi, \eta) \end{bmatrix} = \sum_{i=1}^{M} \begin{bmatrix} x_i \\ y_i \end{bmatrix} \Psi^i(\xi, \eta), \tag{30}$$

where M is the total number of these functions.

Taking the inner products of (1) and (2) at steady state with Φ^i in the melt and solid phases respectively, integrating by parts and adding the resulting equations yields the weak forms of the conservation equation as

$$-\int_{D_m} \nabla C \cdot \nabla \Phi^i \, dA - R_m k \int_{D_s} \nabla C \cdot \nabla \Phi^i \, dA + \int_{D_m} P(\hat{\mathbf{e}}_y \cdot \nabla C) \Phi^i \, dA + k \int_{D_s} P(\hat{\mathbf{e}}_y \cdot \nabla C) \Phi^i \, dA$$
$$+ \int_{\partial D_2} P(1 - C) \Phi^i \, ds + \int_{\partial D_1} (1 - k) C P \hat{\mathbf{e}}_y \cdot \hat{\mathbf{n}} \Phi^i \, ds = 0, \quad i = 1, \ldots, N. \tag{31}$$

Here the boundary conditions (3), (5) and (8)–(10) have been used to resolve boundary integrals that resulted from application of the divergence theorem.[16]

The Gibbs–Thomson equation is discretized by forming inner products with respect to Ψ^i and integrating by parts. Substituting the boundary condition (11) into the resulting equation yields

$$I^i_{GT} = \int_{\partial D_1} \left[(Gy + m/k - mC) \Psi^i + \Gamma \phi \frac{\partial \Psi^i}{\partial s} \right]_{\eta = 0} ds = 0, \quad i = n_1, n_2, \ldots, n_m, \tag{32}$$

where $\{n_i\}$ are the indices of the basis functions which are non-zero at the interface $\eta = 0$.

Although the development of discrete versions of the mapping equations (22) and (24) is analogous to the application of Galerkin's method to the solution of conservation equations, the form of the Gibbs–Thomson boundary condition requires special treatment. The boundary conditions on the domain D for the mapping equations (25)–(27) are incorporated in the weak forms of (22) and (24) to give

$$\int_D (\mathbf{a} \cdot \nabla \eta) \cdot \nabla \Phi^i \, dA + \int_D f(\eta) \Phi^i \, dA + H \int_{\partial D_1} (y + l_s) \Psi^i \, ds$$
$$+ H \int_{\partial D_2} (y - l_m) \Psi^i \, ds + H I^i_{GT} = 0, \quad H \to \infty, \tag{33}$$

$$\int_D \left[\sqrt{\left(\frac{x_\xi^2 + y_\xi^2}{x_\eta^2 + y_\eta^2} \right)} + \varepsilon \right] \nabla \xi \cdot \nabla \Psi^i \, dA + H \int_{\partial D_3} x \Psi^i \, ds + H \int_{\partial D_4} (x - L) \Psi^i \, ds$$
$$+ H \int_{\partial D_1} \left(\xi - \frac{\int_0^\xi \sqrt{(x_{\xi'}^2 + y_{\xi'}^2)} \, d\xi'}{\int_0^1 \sqrt{(x_{\xi'}^2 + y_{\xi'}^2)} \, d\xi'} \right) \Psi^i \, ds = 0, \quad H \to \infty, \tag{34}$$

where the index i is carried over all basis functions $\{\Psi^i\}$, i.e. $i=1, \ldots, M$. The constant H is introduced as a penalty parameter[33] such that $H \gg 1$. Then, if $\Psi^i(\xi, \eta)$ is non-zero on a particular part of the boundary, the residual equations reduce to only the associated boundary conditions. For example, $\Psi^i(\xi, \eta)$ non-zero on ∂D_I gives $I^i_{GT}=0$ for (33).

Accordingly, the coupling between the solidification problem and the mapping problem arises from using the weak formulation of the Gibbs–Thomson equation (32) as an essential boundary condition in the mapping problem. This coupling is consistent with choosing the Gibbs–Thomson condition as the *distinguished boundary condition* in the isotherm/Newton method.[8]

The weak formulation of the solidification/mapping problem given by (31)–(34) is greatly simplified in the transformed co-ordinate system (ξ, η), since all the boundaries appearing in these equations are co-ordinate lines in the transformed system. Thus the calculations of the integrals in the weak formulation are straightforward using the transformation relations in the Appendix.

Equations (31)–(34) are a system of non-linear algebraic equations with $N+2M$ unknowns $\{C_i, x_j, y_j\}$, $i=1, \ldots, N$ and $j=1, \ldots, M$. This set is solved by Newton's method using LU decomposition of the sparse, structured linear equation set that arises at each Newton iteration; frontal matrix-handling methods are used to control storage of the Jacobian matrix. Arc length continuation methods[34] are used to compute families of solutions through folds in the solution space as the parameters (G, P) are varied.

5. RESULTS

The finite element/Newton method for solving the coupled solidification/mapping problem is used here for two sets of model calculations. In the first the calculations of Ungar and Brown[7] for the one-sided solutal model are repeated to resolve the questions posed by Wheeler and Winters.[18] In the second the method is used to repeat the calculations of Ramprasad *et al.*[20] to demonstrate the robustness of the new mapping method for representing cell shapes that evolve from the almost planar interface to cells separated by deep and narrow grooves.

An additional condition has been imposed on the mapping problem in these calculations. A ξ-co-ordinate line close to the interface is required to be horizontal and have a fixed position in the physical domain:

$$y(\xi, \eta) = y^* \quad \text{at } \eta = \eta^*, \ 0 \leqslant \xi \leqslant 1. \tag{35}$$

This constraint results in improved mapping results as the interface deforms, because it partially decouples the mapping of the domain close to the interface from the representation of the far-field domain. An analogous but more flexible constraint has been used in more recent calculations.[35]

The finite element meshes used here have N_ξ elements distributed uniformly in the direction lateral to the interface and $N_\eta = N^m_\eta + N^s_\eta$ elements distributed between melt (N^m_η elements) and solid (N^s_η elements) in the direction of growth. The elements in the melt are graded towards the interface (∂D_I) to help resolve the diffusion layer caused by solute rejection there. The meshes used in specific calculations are listed below.

5.1. *The one-sided solutal model*

The finite element formulation for the one-sided SM is given by (31)–(34) with the integrals over the solid domain and its boundaries omitted. Calculations are for the thermophysical properties that are appropriate for the Pb–Sb alloy, which are given in Table I and are the same as used by Ungar and Brown[7] and more recently by Wheeler and Winters.[18] The dimensionless temperature

Table I. Dimensionless parameters used in the calculations for the one-sided model for directional solidification

Length (L)	1
Growth rate (P)	0·8
Segregation coefficient (k)	0·4
Slope of the liquidus curve (m)	$-1{\cdot}67 \times 10^{-4}$
Capillary constant (Γ)	$8{\cdot}2 \times 10^{-7}$
Ratio of diffusivities in solid and melt	0

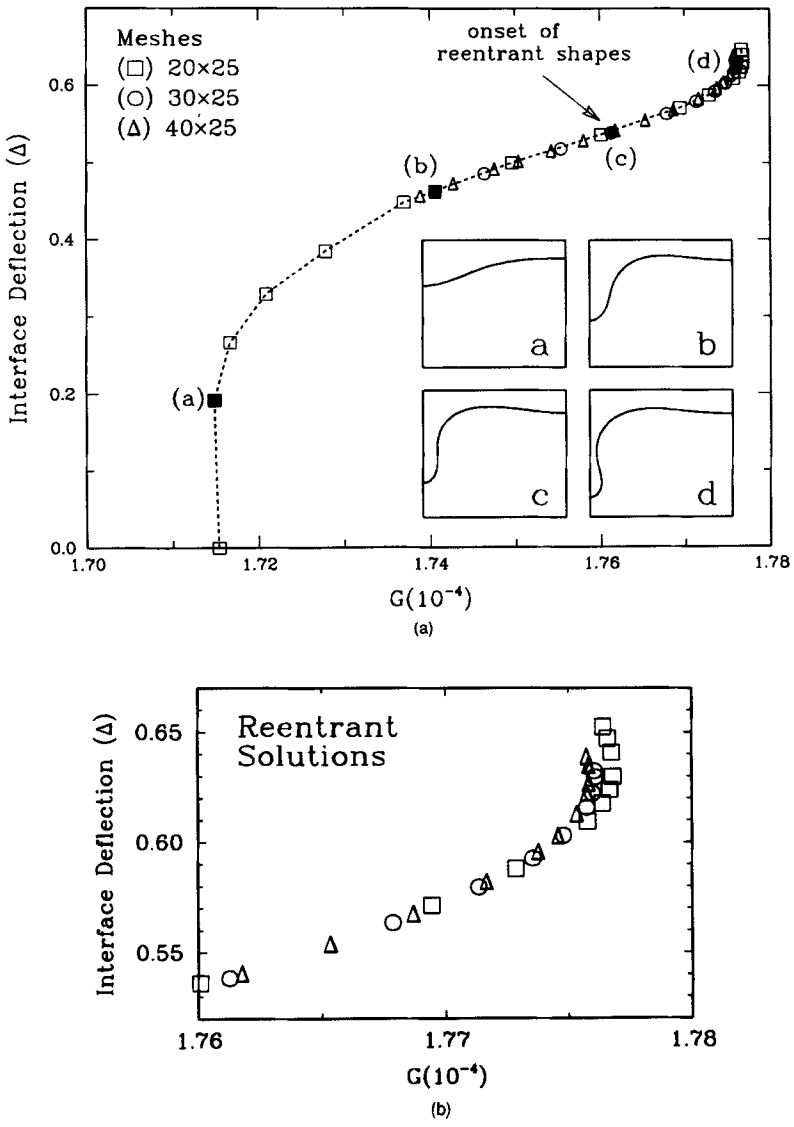

Figure 8. Interface deflection Δ as a function of temperature gradient computed for the one-sided SM and three meshes. Filled symbols and letters refer to the sample cell shapes shown in this figure and the mappings shown in Figure 9.

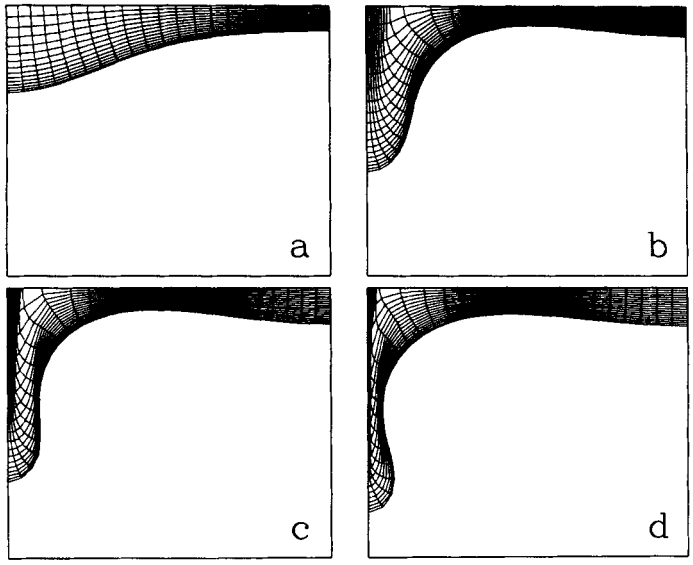

Figure 9. Sample mapping results computed for the one-sided SM and corresponding to the points (a)–(d) of Figure 8(a). Only the region of the melt below the line defined by the constraint (35) is shown.

G is used as a control parameter. For gradients above a critical value G_c the planar interface is the only solution to the problem; however, for $G < G_c$ cellular interface shapes evolve as a bifurcating solution family. The results of Ungar and Brown[7] and Wheeler and Winters[18] for the same set of calculations and a Cartesian Monge interface representation are described in Section 1.

The maximum interface deflection Δ computed with the MMM is summarized in Figure 8(a) for analyses with three finite element meshes: (N_ξ, N_η) values are (25, 20), (25, 30) and (25, 40). Sample interface shapes and mapping results are shown in Figure 9 and correspond to the points (a)–(d) in Figure 8(a). The mapping results of Figure 9 correspond only to the domain between the constraint line and the interface. A sample mapping result for the entire domain is shown in Figure 10.

Cellular shapes bifurcate from the planar state at $G = G_c \approx 1{\cdot}715 \times 10^{-4}$, which agrees with both Ungar and Brown[7] and Wheeler and Winters.[18] The cellular family evolves almost vertically; Wheeler and Winters report that it is slightly supercritical, i.e. as $\Delta \to 0$, the family exists for $G < G_c$. As G is *decreased* from G_c, the cells evolve from a sinusoidal form to have deep grooves and a molar-shaped top.

At $G = 1{\cdot}76 \times 10^{-4}$, marked in Figure 8(a) by point (c), the groove becomes vertical and starts to develop a re-entrant shape. This cell shape is reproduced by calculations with all three meshes. A first point where the family of solutions reverses direction towards increasing values of G is found for $G = 1{\cdot}776 \times 10^{-4}$. Again this solution structure is computed with all three meshes, as shown in Figure 8(b) by the enlargement of this portion of Figure 8(a).

The existence of re-entrant interface shapes explains the failure of the calculations by Ungar and Brown[7] and Wheeler and Winters,[18] since the interface representation used in these analyses does not allow for re-entrant cell shapes. In addition, the calculated re-entrant shapes have another more profound implication on the validity of the predictions of the one-sided SM. As discussed in Section 2, the calculations of re-entrant cells using the one-sided SM are not physically acceptable because the model does not correctly predict the solute concentration of solid that *melts*

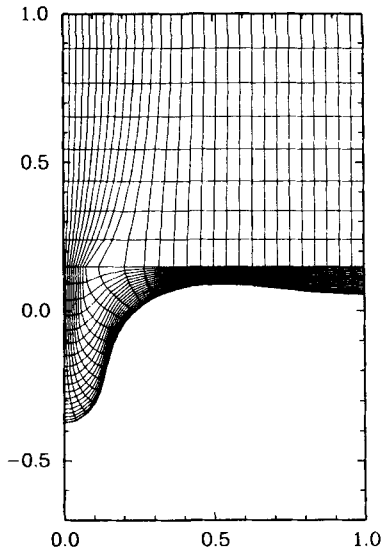

Figure 10. Sample result showing mapping for the entire solidification domain for a calculation (point (c) in Figure 8(a)) with the one-sided SM. The co-ordinates in physical space (x, y) have been included to show that the line constraint was positioned at $y=0{\cdot}15$ along the 17th ξ-curve from the bottom ($\eta=0{\cdot}68$).

in the re-entrant grooves. This limitation is only removed by including solute transport in both phases as in the two-sided model.

5.2. The two-sided solutal model

Meaningful calculations of re-entrant solidification cells and secondary bifurcations that result in halving of the cellular wavelength are demonstrated by calculations for the two-sided solutal model. Again the parameter values are those for the Pb–Sb alloy, except that the diffusivity ratio R_m has been set to unity. The parameter values used are listed in Table II and are the same as used by Ramprasad *et al.*[20] Using finite element calculations based on the Cartesian and the mixed Cartesian/polar interface representations shown in Figure 3(b), these authors demonstrated a sequence of secondary bifurcations with increasing growth rate that split a cell into two and later four cells. Their calculations were carried out on computational domains with L equal to integer fractions of the most dangerous wavelength λ_c.

We have repeated these calculations using the MMM introduced here. The computational domain is kept fixed at $L=\lambda_c/2$ and a mesh with $(N_\xi, N_\eta^m, N_\eta^s)=(100, 20, 20)$ is used. This discretization results in 20 563 non-linear equations and is fine enough in the lateral (ξ) direction to resolve all three solution families with wavelengths λ_c, $\lambda_c/2$ and $\lambda_c/4$ that are expected to form. The bifurcation diagram computed for varying P is shown in Figure 11 as a plot of $\Delta=\Delta(P)$. The secondary bifurcations between interface families with spatially resonant wavelengths are obvious. Sample interface shapes shown in Figure 12 demonstrate the ability of the MMM to represent a variable number of cells in a given sample size. This feature is critical to the effective analysis of tip splitting caused by the codimension-two bifurcation.

These calculations are compared directly with the results of Ramprasad *et al.*[20] for calculations of cells with wavelength $\lambda=\lambda_c/4$. The bifurcation diagram shown in Figure 13 was constructed using three meshes and $L=\lambda_c/8$. The results converge with mesh refinement and show the

Table II. Dimensionless parameters used in the calculations for the two-sided model for directional solidification

Length ($L=\lambda_c/2$)	2·295
Thermal gradient (G)	$4{\cdot}5\times10^{-5}$
Segregation coefficient (k)	0·4
Slope of the liquidus curve (m)	$-1{\cdot}67\times10^{-4}$
Capillary constant (Γ)	$8{\cdot}2\times10^{-7}$
Ratio of diffusivities in solid and melt	1

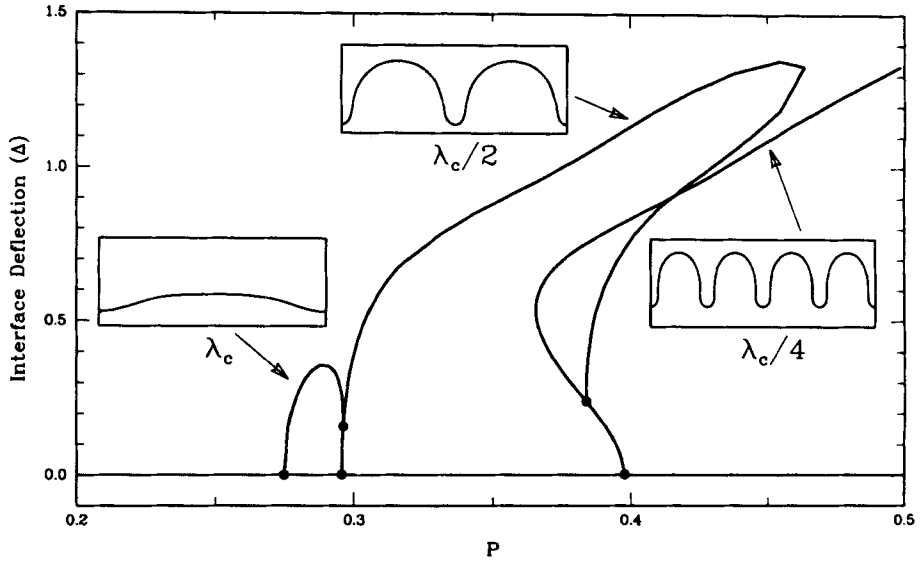

Figure 11. Bifurcation diagram for the two-sided SM. Sample shapes are shown fo the λ_c, $\lambda_c/2$ and $\lambda_c/4$ families.

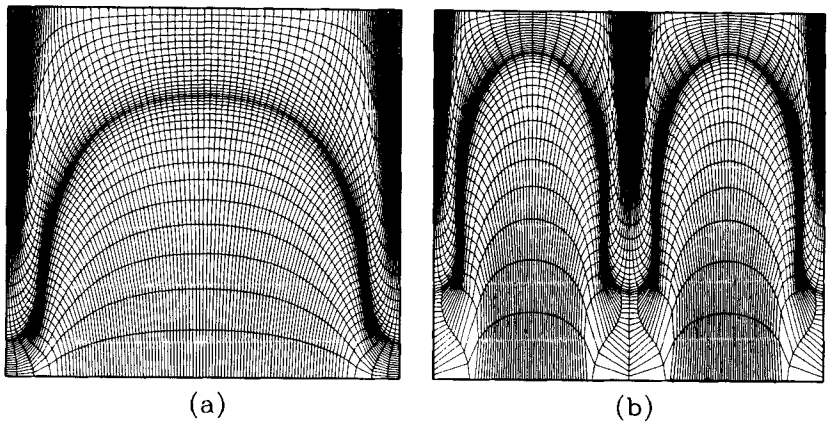

Figure 12. Sample interface shapes and meshes generated for the two-sided SM showing the ability of the MMM to represent a variable number of cells in a given domain. These solutions correspond to (a) $\lambda_c/2$ family, $P=0{\cdot}45$, $\Delta=1{\cdot}166$ and (b) $\lambda_c/4$ family, $P=0{\cdot}47$, $\Delta=1{\cdot}138$.

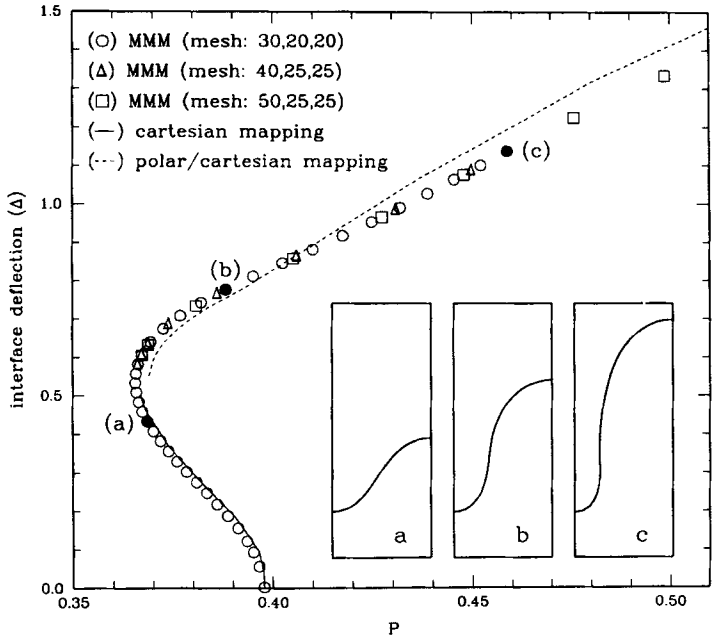

Figure 13. Results from solidification/mapping calculations with the two-sided SM for three meshes. Results from previous calculations by Ramprasad *et al.*[20] are also shown for comparison.

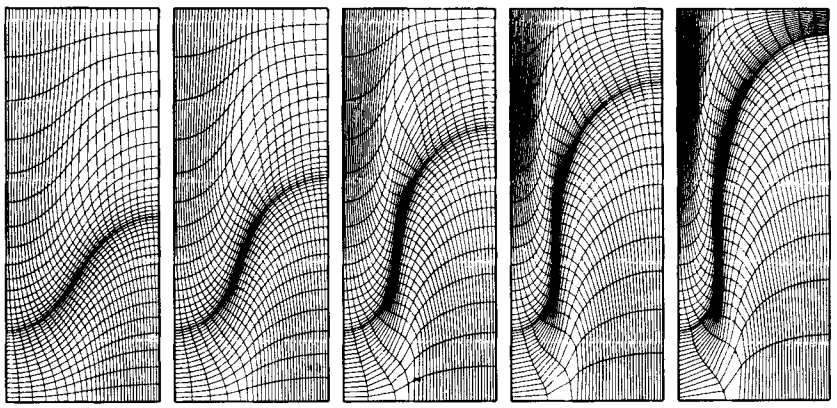

Figure 14. Mapping results for the two-sided SM corresponding to solutions shown in Figure 13.

existence of a limit point in P. These calculations agree well with the results of Ramprasad *et al.*, which also are plotted in Figure 13.

Sample cell shapes and meshes generated by the mapping method are shown in Figure 14. The transition between a relatively shallow and a deep cell is easily approximated by the mapping. The deepest cell ($P=0{\cdot}459$) has an approximately vertical sidewall in the groove. Similar to the

calculations for the one-sided model, constraints on the ξ-curves of the form of (35) have been used above and below the interface at $y = 1{\cdot}15$ and $y = -0{\cdot}35$ respectively. The results shown in Figure 14 are for the part of the domain between these ξ-curves.

6. CONCLUSIONS

Simulations of the development of solidification microstructures are particularly difficult free boundary problems because of the very rapid development of highly deformed cells and grooves and because of the tendency of the number of cells to increase through the tip-splitting mechanism described here and in more detail by Ramprasad *et al.*[20] Numerical analyses based on restrictive representations of the interface can result in erroneous conclusions caused by the failure of the representation to allow for either the tip splitting or the formulation of re-entrant grooves.

The new mapping method described here is capable of approximating these features of the solutions of cellular solidification models. The method is designed specifically to yield a co-ordinate transformation and a mesh that deforms consistently into the deep grooves of cellular structures. This capability of MMM results from the mixture of the direct and variational formulations used to derive equations (22) and (24). In addition, the MMM is general enough to be applied to any other problems where highly distorted interfaces appear.

The results described in Section 5 demonstrate the utility of the mapping method and the robustness of the finite element/Newton method for analysis of cellular interface structures. We show that calculations with the one-sided SM do develop re-entrant cell shapes that cannot be represented by the algebraic Cartesian mapping interface representation used before.[7,18] Hence conclusions reached in these analyses about solution structure are valid only if the slope of the interface is not nearly vertical. An equally important observation is that the one-sided solutal model *is not* a valid description of solute transport when the cell grooves are re-entrant, so that carrying the calculations past this point is meaningless.

The calculations reported in Section 5.2 with the two-sided SM definitely demonstrate the secondary bifurcations that cause wavelength halving in cellular solidification by verifying previous predictions.[16] These results also demonstrate the robustness of the mixed mapping method to compute the evolution in the number of cells in the sample caused by tip splitting. The presence of these secondary bifurcations was linked by Ungar and Brown[7] to the presence of a codimension-two bifurcation point for cellular structures with a nearly fundamental wavelength λ; calculations in a sample with size L near this value resulted in shifting the secondary bifurcation to cells with lower deflection (smaller Δ) that can be resolved by the Monge representation. Similar results are reported elsewhere.[17]

In the finite element formulation described in Section 4 a lower-order approximation (bilinear elements) is used for the unknowns (x, y) of the mapping problem than the approximation used for the concentration field (biquadratic elements). The use of this subparametric mapping is justified since the degree of accuracy to which the mapping equations are solved does not affect the accuracy of the concentration field, which is the physical unknown of interest. However, at the interface the mapping problem is coupled to the solidification problem through the Gibbs–Thomson equation. Here, due to the subparametric mapping, the degrees of freedom allowed for the position (x, y) of the interface are only half as many as those allowed for the concentrations along the interface. Hence error due to poor approximation of the interface position could corrupt the accuracy of the concentration field. This limitation can be removed by incorporating transition finite element approximations[36] for the elements adjacent to the interface instead of using bilinear elements for the unknowns (x, y). These elements reduce to

quadratic approximations along the side adjacent to the interface and to linear approximations along the remaining three sides, allowing for both quadratic approximation of the interface shape and subparametric mapping for the rest of the domain.

The generality of the mixed mapping method leads to added expense of the solution of the mapping equations (22) and (24) throughout the two-dimensional domain, instead of the calculation of a one-dimensional shape function which characterizes an algebraic mapping method. This expense is especially significant for solution of the SM of microstructure solidification which is described by a single field equation. This increase is offset slightly by using lower-order finite element representations for the mapping variables (30) than for the concentration variables (29). This incremental expense is smaller when more field equations are solved, as is the case in viscous free surface flows[9-12] and in analyses of solidification systems with convection.[37,38] Application of the mapping method to these classes of problems is under way.

Note Added in Proof

While this article was in proof Christodoulou and Scriven[39] pointed out that the mapping equations (20) and (21) should be used with $\varepsilon_1 < 0$ and $\varepsilon_2 < 0$, instead of the positive values reported in Reference 10. In this case the combination of the orthogonality and concentration control terms does not alone change the mathematical type and the mapping can be used successfully without the contribution from the smoothness functional. We performed calculations using equations (20) and (21) with $\varepsilon_1 < 0$, $\varepsilon_2 < 0$ and $0 < \varepsilon \ll 1$ for the domains shown in Figure 6 and the results were satisfactory for a suitable choice of the function $g(\eta)$ in equation (21). However, we have not been able to create satisfactory maps using this version of equations (20) and (21) for the domains shown in Figure 7(b).

ACKNOWLEDGEMENTS

This Research was supported by the National Science Foundation and by the United States National Aeronautics and Space Administration. Computational resources were supplied by a grant from the Pittsburg National Supercomputer Center.

APPENDIX: CONVERSION OF VARIATIONAL EQUATIONS TO TRANSFORMED CO-ORDINATES

The surface and line integrals appearing in the fomulation of Section 4 are calculated using the following rules for any function $g(\xi, \eta)$:

$$\int_D g \, dA = \int_{-1}^{1} \int_{0}^{1} gJ \, d\xi \, d\eta,$$

$$\int_{\partial D_{1,2}} g \, ds = \int_{0}^{1} [g q_\xi]_{\eta = -1,1} \, d\xi,$$

$$\int_{\partial D_{3,4}} g \, ds = \int_{-1}^{1} [g q_\eta]_{\xi = 0,1} \, d\xi,$$

$$\int_{\partial D_1} g \, ds = \int_{0}^{1} [g q_\xi]_{\eta = 0} \, d\xi,$$

where

$$q_\xi \equiv \sqrt{(x_\xi^2 + y_\xi^2)}, \qquad q_\eta \equiv \sqrt{(x_\eta^2 + y_\eta^2)}, \qquad J \equiv x_\xi y_\eta - x_\eta y_\xi.$$

The gradient operator is transformed as

$$\nabla g = J^{-1}[(g_\xi y_\eta - g_\eta y_\xi)\hat{\mathbf{e}}_x + (g_\eta x_\xi - g_\xi x_\eta)\hat{\mathbf{e}}_y].$$

The melt/solid interface is described by the curve $\eta(x, y) = 0$ and, according to (4), the unit vector normal to the interface is

$$\hat{\mathbf{n}} \equiv \left[\frac{\nabla\eta}{|\nabla\eta|}\right]_{\eta=0} = \left[\frac{-y_\xi\hat{\mathbf{e}}_x + x_\xi\hat{\mathbf{e}}_y}{q_\xi}\right]_{\eta=0}.$$

The derivative of a function $g(\xi, \eta)$ with respect to the arc length along the interface is given by

$$\left[\frac{dg}{ds}\right]_{\eta=0} = \left[\frac{g_\xi}{q_\xi}\right]_{\eta=0}.$$

REFERENCES

1. W. A. Tiller, K. A. Jackson, J. W. Rutter and B. Chalmers, 'The redistribution of solute atoms during the solidification of metals', *Acta Metall.*, **1**, 428–437 (1953).
2. M. A. Eshelman, V. Seetharaman and R. Trivedi, 'Cellular spacings—I. Steady-state growth', *Acta Metall.*, **36**, 1165–1174 (1988).
3. V. Seetharaman, M. A. Eshelman and R. Trivedi, 'Cellular spacings—II. Dynamical studies', *Acta Metall.*, **36**, 1175–1185 (1988).
4. D. P. Woodruff, *The Solid–Liquid Interface*, Cambridge University Press, Cambridge, 1973.
5. W. W. Mullins and R. F. Sekerka, 'Stability of a planar interface during solidification of a dilute binary alloy', *J. Appl. Phys.*, **35**, 444–451 (1964).
6. D. J. Wollkind and L. A. Segel, 'A nonlinear stability analysis of the freezing of a dilute binary alloy', *Phil. Trans. R. Soc. Lond.*, **268**, 351–380 (1970).
7. L. H. Ungar and R. A. Brown, 'Cellular interface morphologies in directional solidification. The one sided model', *Phys. Rev. B*, **30**, 1367–1380 (1984).
8. H. M. Ettouney and R. A. Brown, 'Finite-element methods for steady solidification problems', *J. Comput. Phys.*, **49**, 118–150 (1983).
9. S. F. Kistler and L. E. Scriven, 'Coating flows', in J. R. A. Pearson and S. M. Richardson (eds), *Computational Analysis of Polymer Processing*, Applied Science, Essex, 1983, pp. 243–299.
10. K. N. Christodoulou and L. E. Scriven, 'Discretization of free surface flows and other moving boundary problems', University of Minnesota Supercomputer Institute, UMSI 88/129, Minneapolis, 1988.
11. G. Ryskin and L. G. Leal, 'Numerical solution of free-boundary problems in fluid mechanics. Part 1. The finite-difference technique', *J. Fluid Mech.*, **148**, 1–17 (1984).
12. G. Ryskin and L. G. Leal, 'Numerical solution of free-boundary problems in fluid mechanics. Part 2. Buoyancy-driven motion of a gas bubble through a quiescent liquid', *J. Fluid Mech.*, **148**, 19–35 (1984).
13. D. S. Dandy and L. G. Leal, 'A Newton's method scheme for solving free-surface flow problems', *Int. j. numer. methods fluids*, **9**, 1469–1486 (1989).
14. J. F. Thompson, Z. U. A. Warsi and C. W. Mastin, 'Boundary-fitted coordinate systems for numerical solution of partial differential equations—A review', *J. Comput. Phys.*, **47**, 1–108 (1982).
15. J. F. Thompson, Z. U. A. Warsi and C. W. Mastin, *Numerical Grid Generation*, North-Holland, Amsterdam, 1985.
16. L. H. Ungar, N. Ramprasad and R. A. Brown, 'Finite element methods for unsteady solidification problems arising in prediction of morphological structure', *J. Sci. Comput.*, **3**, 77–108 (1988).
17. M. J. Bennett and R. A. Brown, 'Cellular dynamics during directional solidification: interaction between multiple cells', *Phys. Rev.*, **39**, 11705–11723 (1989).
18. A. A. Wheeler and K. H. Winters, 'On a finite element method for the calculation of steady cellular interfaces in the one-sided model of solidification', *Commun. Appl. Numer. Methods*, **5**, 309–320 (1989).
19. L. H. Ungar and R. A. Brown, 'Cellular interface morphologies in directional solidification. IV. The formation of deep cells', *Phys. Rev. B*, **31**, 5931–5940 (1985).
20. N. Ramprasad, M. J. Bennett and R. A. Brown, 'Wavelength dependence of cells of finite depth in directional solidification', *Phys. Rev.*, **38**, 583–592 (1988).
21. C. E. Weatherburn, *Differential Geometry in Three Dimensions*, Cambridge University Press, Cambridge, 1927.

22. K. J. Ruschak, 'A method for incorporating free boundaries with surface tension in finite elements fluid-flow simulations', *Int. j. numer. methods eng.*, **15,** 639–648 (1980).
23. Y. Saito, Goldbeck-Wood and H. Muller-Krumbhaar, 'Numerical simulation of dendritic growth', *Phys. Rev. A*, **38,** 2148–2157 (1988).
24. G. Ryskin and L. G. Leal, 'Orthogonal mapping', *J. Comput. Phys.*, **50,** 71–100 (1980).
25. R. Aris, *Tensors, Vectors, and the Basic Equations of Fluid Mechanics*, Dover, New York, 1989.
26. J. F. Thompson, F. C. Thames and C. W. Mastin, 'Automatic numerical generation of body-fitted curvilinear coordinates system for field containing any number of arbitrary two-dimensional bodies', *J. Comput. Phys.*, **15,** 299–319 (1974).
27. P. R. Eiseman, 'Orthogonal grid generation', in J. C. Thompson (ed.), *Numerical Grid Generation*, North-Holland, Amsterdam, pp. 193–233.
28. R. Menikoff and C. Zemach, 'Methods for numerical conformal mapping', *J. Comput. Phys.*, **36,** 366–410 (1980).
29. J. U. Brackbill and J. S. Saltzman, 'Adaptive zoning for singular problems in two dimensions', *J. Comput. Phys.*, **46,** 342–368 (1982).
30. J. L. Troutman, *Variational Calculus with Elementary Convexity*, Springer, New York, 1983.
31. R. I. Kreis, F. C. Thames and H. A. Hassan, 'Application of a variational method for generating adaptive grids', *AIAA J.*, **24,** 404–410 (1986).
32. G. F. Carrier and C. E. Pearson, *Partial Differential Equations, Theory and Technique*, Academic, New York, 1976.
33. G. Strang and G. J. Fix, *An Analysis of the Finite Element Method*, Prentice-Hall, Englewood Cliffs, NJ, 1973.
34. Y. Yamaguchi, C. J. Chang and R. A. Brown, 'Multiple buoyancy-driven flows in a vertical cylinder heated from below', *Phil. Trans. R. Soc. Lond. A*, **312,** 519–552 (1984).
35. K. Tsiveriotis and R. A. Brown, 'Solution of free boundary problems using finite element/Newton methods and locally refined grids: application to analysis of solidification microstructure', *Int j. numer. methods fluids*, submitted.
36. G. F. Carey and J. T. Oden, *Finite Elements, Vol. I*, Prentice-Hall, Englewood Cliffs, NJ, 1981.
37. P. M. Adoranto and R. A. Brown, 'Convection and segregation in directional solidification of dilute and non-dilute binary alloys: effects of ampoule and furnace design', *J. Cryst. Growth*, **80,** 155–190 (1987).
38. P. A. Sackinger, R. A. Brown and J. J. Derby, 'A finite element method for analysis of fluid flow, heat transfer and free interfaces in Czochralski crystal growth', *Int. j. numer. methods fluids*, **9,** 453–492 (1988).
39. K. N. Christodoulou and L. E. Scriven, 'Discretization of free interface flows and other moving boundary problems', *J. Comp. Phys.*, in press (1992).